[1.] Vanja MANDRIĆ, [2.] Slavko RUPČIĆ, [3.] Bogdan PAVKOVIĆ, [4.] Dina JUKIĆ

ELECTRIC FIELD STRENGTH DISTRIBUTION OF AN ECCENTRIC RING RESONATOR AT MICROWAVE FREQUENCIES

[1,2.] Department of Communication; Faculty of Electrical Engineering, Computer Science and Information Technology Osijek; Osijek, CROATIA
[3.] Department of Computing and Control Engineering; Faculty of Technical Sciences University of Novi Sad; Novi Sad, SERBIA
[4.] Department of Core Courses, Faculty of Electrical Engineering, Computer Science and Information Technology; Osijek; Osijek, CROATIA

Abstract: Paper presents a numerical investigation of the electric field distribution on and behind a ring resonator operating at frequencies below 1 GHz. This study is a continuation of previous research, with a particular focus on the spatial distribution of the electric field on the resonator: in the region behind it, and at the receiving antenna. The ring resonator is positioned at an incident angle of 0° relative to the incoming electromagnetic wave, allowing a clear assessment of its interaction with the incident field under normal incidence conditions. The main contribution of this work is the comparative analysis of field behavior at different characteristic frequencies. The results confirm that the ring resonator exhibits the strongest field absorption at its first resonant frequency, where the electric field is predominantly concentrated along the ring structure, resulting in a significant reduction of the transmitted field behind the resonator and at the receiving antenna. At the second resonant frequency, the field absorption on the ring is lower, allowing a larger fraction of energy to reach the receiving antenna. At a non-resonant frequency, the ring shows minimal excitation, effectively allowing the strongest field to propagate to the receiving antenna, as the resonator no longer confines energy. All simulations were conducted using ANSYS HFSS v.221, enabling full-wave electromagnetic analysis of the modelled structure. In addition, the results contribute to a better understanding of resonance-driven field localization and attenuation mechanisms in sub-1 GHz ring resonator configurations, with potential relevance for electromagnetic field control and shielding applications.
Keywords: protection from EM radiation, ring resonator, resonant frequencies, electric field strength distribution

1. INTRODUCTION

The rapid expansion of wireless communication technologies over recent decades has significantly increased public and scientific attention to electromagnetic (EM) field exposure and its potential effects. Systems operating below 1 GHz, such as legacy broadcasting and mobile communication services, remain widely deployed, while newer generations including 4G, 5G NR, and the emerging 6G paradigm continue to expand the overall electromagnetic spectrum occupancy. This accelerated technological development requires not only regulatory compliance and technical optimization, but also greater user awareness and responsible engineering approaches aimed at mitigating unwanted electromagnetic exposure.

Among available protection strategies, electromagnetic shielding has proven to be one of the most effective methods for controlling field propagation and reducing exposure levels. Conventional shielding solutions typically rely on continuous conductive enclosures or multilayer materials. However, recent research trends emphasize the development of frequency-selective and resonance-based structures that enable targeted attenuation at specific frequency bands. These approaches offer the advantages of tailored electromagnetic response, improved efficiency, and potentially reduced material usage.

In this context, ring resonators represent a promising solution for frequency-selective electromagnetic control. When properly designed, their geometrical parameters: radius, width, and substrate configuration, can be tuned to resonate at predefined frequencies. This enables selective interaction with incident electromagnetic waves and enhanced field localization at resonance. In particular, structures operating in the sub-1 GHz range are of considerable practical relevance due to the continued presence of communication and broadcasting systems within this band.

The main contribution of this paper is a detailed and systematic investigation of the electric field distribution on the ring resonator and in the region behind the resonator at frequencies below 1 GHz. Special emphasis is placed on analyzing field behavior at the first and the second resonant frequencies, as well as at a selected non-resonant frequency, to clearly distinguish resonance-driven effects from general propagation phenomena. By thoroughly examining spatial field localization, attenuation characteristics, and field levels at the receiving antenna, this work provides deeper insight into the physical mechanisms governing resonance-based shielding performance.

The results show how the geometrically optimized resonant structures contribute to efficient, frequency-selective electromagnetic shielding. This is essential for the development of advanced protective solutions compatible with the evolving electromagnetic environment.

2. RELATED WORK

Recent research in electromagnetic field control increasingly focuses on developing resonant and metasurface-based structures for sensing and shielding applications. In most cases, primary emphasis is placed on scattering parameters, transmission and reflection coefficients, and overall shielding effectiveness (SE) as key performance indicators. These approaches provide valuable quantitative insight into attenuation capabilities; however, they often offer limited understanding of the underlying field interaction mechanisms responsible for resonance-driven behavior.

The authors in [1] investigate the installation of split-ring resonators in textile materials for shielding effectiveness enhancement, and show the purpose of resonators at target frequencies. The authors' awareness of the health impacts and effects of existing wireless technologies is also analyzed in [2], which provides a general overview of resonators, their advantages and disadvantages, the materials involved, production techniques, processes, and applications. Reference [3] presents the concept, implementation, and analysis of a miniature metamaterial (MTM) unit cell for sub-6 GHz applications in fifth generation mobile technology. The design features a circular split resonator with two parallel copper elements at the front and a slotted rectangular element at the back to form the metamaterial. This configuration achieves a resonant frequency of 3.5 GHz. Boland et al. [4] describe a technique for implementing complementary split ring resonators (CSRR) in frequency selective surfaces (FSS). Their focus is on the practical implementation of resonant structures for RF applications, including control of reflection and transmission. In [5] a microwave sensor based on a split ring resonator (SRR) operating at 2.5 GHz, printed on a biodegradable cellulose acetate (CA) substrate is presented. The study examines the influence of the feed position and ring geometry on the possible resonant frequencies and transmission amplitude in detail.

The developed sensors provide a promising solution for cost-effective and sustainable microwave sensing applications. Islam et al. present a multiband SRR sensor based on an asymmetric cross-split ring resonator that achieves four resonant frequencies. The electric field and scattering parameters (S-parameters) are analyzed. Their study demonstrates how geometric and electromagnetic modifications enable multiple resonances, which is relevant for frequency-selective shielding [6]. In [7], the authors discuss an electromagnetic shield based on a miniaturized frequency selective surface (FSS) for reducing the electromagnetic field in the X-band. The structure uses resonant elements that enable selective attenuation without completely blocking the spectrum. Furthermore, Meka and Shambavi [8] present a conformal ultra-thin single-layer band stop and band pass FSS for microwave applications. The FSS consists of two concentric rectangular rings (CCSR) and two convoluted rectangular rings (CVSR), and the performance and shielding effectiveness (SE) are verified in an anechoic chamber. Also, simulations and measurements are in good agreement and high SE is achieved in the 5G NR spectrum. Also, in [9], EM protection is proposed by designing a planar frequency-selective metasurface (FSMS) that operates in the WLAN and X-band frequency ranges. Finally, the authors whose work is further explored in this contribution, explain how the eccentric ring resonator operates, how resonant frequencies are achieved, and the purpose of the ring resonator in [10].

Based on the reviewed literature, although resonant and metasurface structures have been extensively investigated in terms of scattering parameters and overall shielding performance, detailed spatial analysis of electric field distribution remains limited, particularly in the sub-1 GHz frequency range. This gap is especially relevant when resonance-driven field localization is considered the dominant mechanism governing attenuation.

The following sections present a comprehensive theoretical and numerical investigation of the electric field distribution on the ring resonator and in the region behind the resonator. The analysis focuses on frequencies below 1 GHz, including both resonant and non-resonant operating points. Special emphasis is placed on visualizing and quantifying field localization effects in order to better understand the physical mechanisms responsible for frequency-selective attenuation.

ISSN 1584 – 2665 (printed version); ISSN 2601 – 2332 (online); ISSN-L 1584 – 2665

3. THEORETICAL BACKGROUND OF THE RING RESONATOR STRUCTURE

The primary objective of ring resonator analysis is to achieve an optimized electromagnetic response through a carefully controlled and geometrically tailored design. When properly dimensioned, resonant structures enable selective interaction with incident electromagnetic waves, allowing controlled field localization and attenuation at predefined frequencies. Such design-oriented approach is essential when resonance phenomena are exploited for practical electromagnetic field management.

In this study, the ring resonator is considered as a frequency-selective structure intended for electromagnetic field mitigation in environments where people live and work. The increasing density of radiofrequency sources requires engineering solutions capable of reducing unwanted field exposure while preserving functional communication bands. Resonance-based structures represent an efficient approach because their electromagnetic response can be precisely tuned via geometrical parameters.

Various ring resonator configurations have been proposed in the literature, including single-ring, split-ring, concentric, and complementary geometries. The structure investigated in this work consists of two circular rings connected at a single point (see Figure 1.), forming an eccentric ring resonator configuration. The eccentricity introduces asymmetry into the structure, influencing current distribution, field localization, and resonant behavior.

The targeted frequency range in this research is below 1 GHz, where numerous active radio systems operate, including FM broadcasting, DVB-T2 digital television, and sub-6 GHz 5G NR services. As these systems remain widely deployed and continuously active, understanding and controlling electromagnetic field behavior within this frequency band is of particular practical relevance.

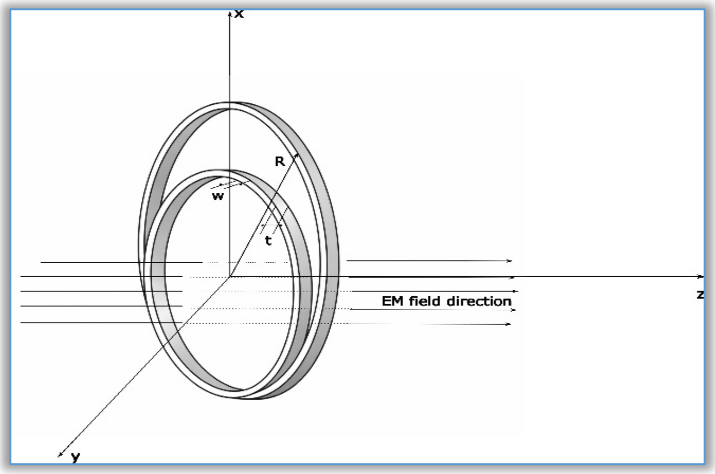

Figure 1. Eccentric ring resonator and its geometric parameters: R- radius, t- depth of the ring, and w- ring width

To enable the ring resonator to attenuate the electromagnetic (EM) field at the desired frequencies, it is essential to determine the resonant frequencies of the structure.

The resonant frequencies are those at which the ring exhibits its strongest electromagnetic response. In practice, these frequencies are identified by the minimum value of the transmission coefficient, S_{21}. The lowest magnitude of the S_{21} parameter occurs at the resonant frequencies, which can be calculated as follows [10]:

$$2\pi R = m\lambda_m \quad (1)$$

$$f_m = \frac{mc}{2\pi R\sqrt{\varepsilon_{eff}}}, \quad (2)$$

where $2\pi R$ represents the circumference of the ring resonator, calculated as an integer multiple of the wavelength; the resonant frequency corresponding to this integer is f_m, whereas c is the speed of light in free space, and ε_{eff} is the effective dielectric constant (approximately equal to unity for free space). All of the above applies to a conducting ring of radius R [10]. Equations (1) and (2) are valid for calculation of the resonant frequency, which importance is due to the fact the ring is affected by an incident electromagnetic wave of different frequencies. Only at resonant frequencies does the ring resonator absorb the wave energy and prevent it from passing to the receiving observation point.

The resonant frequencies of the structure are directly governed by the geometric parameters of the outer and inner rings. Variations in their characteristic dimensions result in corresponding shifts of the resonance positions. Specifically, the outer (larger) ring predominantly determines the lower resonant frequency, while the inner (smaller) ring primarily controls the higher resonant frequency. By applying equations (1) and (2), the target resonant frequencies were calculated, and the obtained values are summarized in Tables 1 and 2.

Table 1. Analytical determination of resonant frequencies (MHz) for the first mode of ring resonator with different outer radius *R* - large (outer) resonator ring.

R, mm	Resonant frequency for the first mode m = 1, MHz
85	561.30
95	502.30
105	454.40

Table 2. Analytical determination of resonant frequencies (MHz) for the first mode of ring resonator with different outer radius R - small (inner) resonator ring.

R, mm	Resonant frequency for the first mode m = 1, MHz
56.5	844.90
66.5	717.50
76.5	623.80

In this study, the analysis is restricted to the frequency range below 1 GHz; therefore, Tables 1 and 2 present results exclusively for the fundamental mode (m=1). The same analytical procedure and calculation methodology are directly applicable to higher-order modes (i.e., higher frequency ranges). However, these are beyond the scope of the present work.

The parameter values listed in the aforementioned tables were subsequently used as input data for the numerical simulations performed in ANSYS HFSS v.221, enabling the solution and validation of the proposed structure.

Tables 1 and 2 summarize the calculated resonant frequencies corresponding to selected values of the outer and inner ring radii. It should be noted, however, that slight deviations in these frequencies may occur when the effective ring radius is considered, together with the influence of the ring thickness and depth. The complete theoretical background and detailed mathematical formulation of this approach have been presented in our previous work; therefore, the derivation is not repeated here. For a comprehensive description of the methodology, the reader is referred to reference [10].

For the subsequent numerical investigation of the electromagnetic field distribution, the authors adopted the parameter values reported in the tables, together with the corresponding geometric parameters of the ring resonator.

4. PARAMETERS REQUIRED FOR NUMERICAL SIMULATIONS

This section presents the numerical analysis of the electromagnetic field distribution near the ring resonator, with particular emphasis on the electric field intensity on the resonator structure itself and in the region behind it. All simulations were carried out using ANSYS HFSS, a FEM-based full-wave electromagnetic solver extensively used for analyzing high-frequency structures.

The numerical model was configured so that the ring resonator was positioned between two antennas, forming a transmission setup suitable for evaluating its attenuation performance. The geometry and antenna placement were defined to satisfy the far-field condition for both antennas, ensuring proper plane-wave illumination of the resonator and reliable evaluation of the transmitted field.

The analysis included the calculation of the transmission coefficient S_{21}, as well as the spatial distribution of the electric field magnitude on the resonator surface and in the region behind the structure (i.e., in the direction of wave propagation). The simulations were conducted at three characteristic frequencies: the first resonant frequency (f_{res1}), the second resonant frequency (f_{res2}) (both previously determined in the analytical section), and one non-resonant frequency (f_{non_res}) selected for comparison.

This approach enables direct assessment of the resonator's influence on field attenuation at resonance, as well as evaluation of its behavior outside the resonant regime, providing comprehensive insight into its electromagnetic performance.

The ring resonator was oriented at an incidence angle of 0°relative to the incoming electromagnetic wave, ensuring horizontal wave excitation. The simulation configuration is shown in Figure 2. As mentioned previously, the analyzed structure is a ring resonator defined by the following geometric parameters:

- R_1 - the outer ring radius,
- R_2 - the inner ring radius,
- t - the thickness (depth) of the rings,
- w - the ring width.

ISSN 1584 – 2665 (printed version); ISSN 2601 – 2332 (online); ISSN-L 1584 – 2665

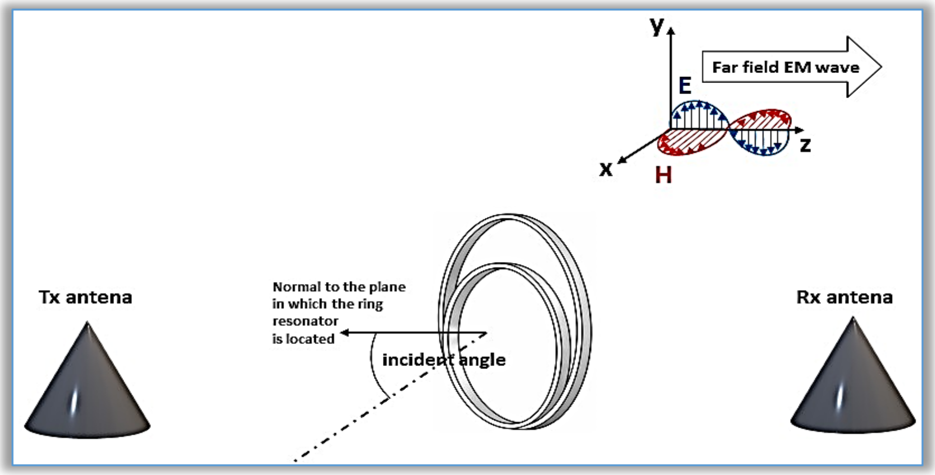

Figure 2. Electromagnetic wave interacting with antennas (Tx is port one, and Rx is port 2).

The last two parameters refer to geometric characteristics common to both concentric rings. For the purposes of this study, knowledge of the radius (R_1) and (R_2) is sufficient to determine the desired resonant frequencies, and the corresponding values can be calculated using equations (1) and (2). The specific values of these parameters, shown in Table 3, are chosen so that the first two resonant frequencies, f_{res1} and f_{res2}, are achieved. At these frequencies, a detailed analysis of the transmission coefficient S_{21} and the corresponding electric field strength distribution E is carried out to evaluate the electromagnetic response of the structure.

Table 3. Geometrical parameters of the ring resonator corresponding to the first two resonant frequencies.

R_1, mm	R_2, mm	f_{res1}, MHz	f_{res1}, MHz
95.00	66.50	502.30	717.50

5. NUMERICAL SIMULATIONS AND CALCULATION OF THE TRANSMISSION COEFFICIENT S_{21} AND ELECTRIC FIELD STRENGTH E

Calculation and graphical representation of the transmission coefficient S_{21}

The analysis begins with the evaluation of the transmission coefficient S_{21}, as it serves as the primary indicator of the resonator's transmission and attenuation characteristics. Since S_{21} quantifies the ratio of the transmitted to the incident signal between the input and output ports, it provides direct insight into the frequency-dependent response of the structure. In Figure 2, the Tx antenna represents the transmitting port (Port 1), whereas the Rx antenna represents the receiving port (Port 2) used for the evaluation of the transmission coefficient S_{21}.

The resonant frequencies are identified by pronounced minima in the magnitude of S_{21}, corresponding to maximum attenuation of the transmitted wave. Establishing the behavior of S_{21} is therefore a necessary first step before proceeding to a detailed spatial analysis of the electric field distribution E, enabling a comprehensive interpretation of the resonator's electromagnetic performance.

The first step is to calculate the transmission coefficient S_{21}. Figure 3 shows the S_{21} response corresponding to the geometric parameters specified in the previous section. The same figure also includes a reference curve representing the scenario without a ring resonator between the two antennas, as well as an additional curve illustrating the contribution of the ring resonator to the reflection coefficient.

As shown in Figure 3, two pronounced minima are observed in the transmission response, corresponding to the desired resonant frequencies f_{res1} = 410.00 MHz and f_{res2} = 708.00 MHz. The numerically calculated transmission coefficient values at these frequencies are $S_{21}(f_{res1})$ = −49.31 dB and $S_{21}(f_{res2})$ = −32.23 dB, respectively.

To accurately quantify the attenuation introduced by the ring resonator, the transmission response obtained with the resonator is compared to the reference case without the resonator placed between the antennas. The resulting differences are −13.35 dB at f_{res1} and −3.61 dB at f_{res2}, representing the net attenuation contribution of the resonator structure. The significantly greater attenuation observed at the first resonant frequency indicates stronger energy confinement and higher electromagnetic interaction between the incident wave and the larger ring. In contrast, the second resonance exhibits a weaker attenuation effect, suggesting reduced field localization and lower energy storage within the structure at that frequency.

ISSN 1584 – 2665 (printed version); ISSN 2601 – 2332 (online); ISSN-L 1584 – 2665

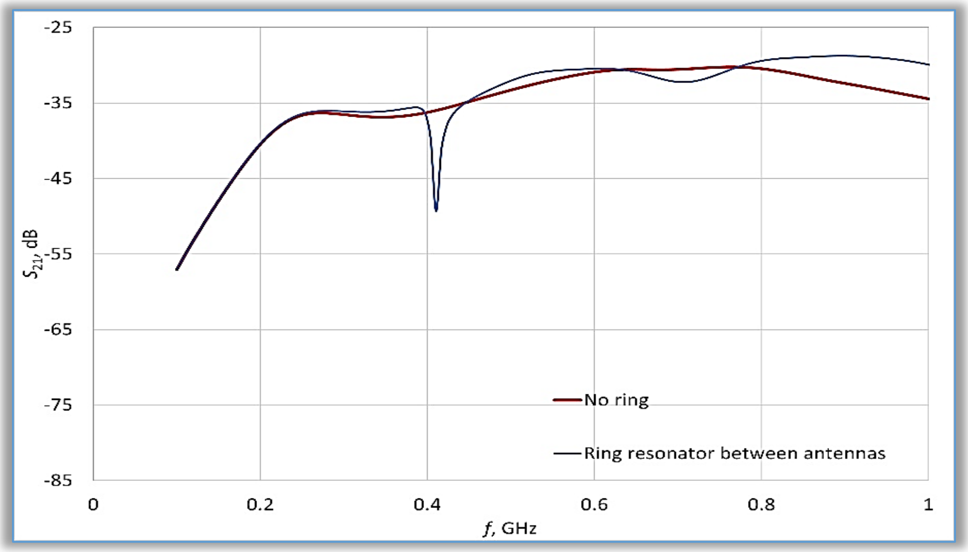

Figure 3. Transmission coefficient S_{21} for two configurations: in red, without a ring resonator (free space), and in blue, with a ring resonator placed between the antennas.

It should be noted that small discrepancies are observed between the analytically calculated and numerically simulated resonance frequencies. For the structure considered, the full-wave simulation yielded resonance frequencies of f_{res1} = 410.00 MHz and f_{res2} = 708.00 MHz, whereas the analytical calculation produced f_{res1} = 502.00 MHz and f_{res2} = 710.00 MHz. As seen in Figure 3, the second resonance frequency coincides almost exactly, while the slight deviation in the first resonance is attributed to the approximations inherent in the analytical model. Such differences are common when comparing simplified analytical formulas with full-wave electromagnetic simulations. This type of analytical calculation does not take into account the coupling (inductive and capacitive), which is the main reason for the deviation. However, this is addressed in [10].

Calculation and graphical representation of electric field strength E

While the transmission coefficient S_{21} provides a quantitative measure of the attenuation characteristics of the ring resonator, it does not offer sufficient insight into the physical mechanisms responsible for this behavior. Therefore, a detailed analysis of the electric field strength distribution is required to understand the interaction between the incident electromagnetic wave and the resonant structure.

The spatial distribution of the electric field allows identification of regions of field concentration, energy localization, and possible field enhancement effects occurring under resonant conditions. In particular, at resonant frequencies, strong field confinement is expected in specific regions of the ring, reflecting efficient energy storage and increased electromagnetic coupling. Thus, examining the electric field magnitude on the resonator surface and in the region behind the structure provides a deeper physical interpretation of the attenuation phenomena previously observed in the S_{21} response. The corresponding electric field distributions are illustrated in Figure 4(a)-(c).

Figure 4(a) shows the spatial distribution of the electric field magnitude at the first resonant frequency. A pronounced field concentration is observed along the outer ring circumference, where the electric field reaches its maximum values (red region, up to approximately 200 V/m according to the scale). The field distribution indicates strong localization of electromagnetic energy within the ring structure. The outer ring exhibits dominant excitation, while the inner region shows comparatively lower field intensity. This behavior confirms that, at f_{res1}, the structure operates in a resonant mode characterized by efficient energy storage and strong coupling with the incident electromagnetic wave. Moreover, a noticeable attenuation of the field behind the resonator is observed, as indicated by the gradual transition towards lower field magnitudes (green to blue regions). This confirms that a significant portion of the incident energy is confined and absorbed within the resonant structure rather than transmitted further, which is consistent with the previously observed minimum in the S_{21} parameter. The high degree of field confinement and the strong intensity contrast between the resonator and the surrounding region explain the substantial attenuation (−13.35 dB) obtained at this resonant frequency.

Figure 4(b) shows the electric field magnitude at the second resonant frequency. Unlike Figure 4(a), the field intensity is noticeably lower, with no pronounced red regions and significantly reduced peak values. Although field localization remains visible along the ring structure, the confinement effect is weaker and more spatially distributed. The electric field is less concentrated on the outer ring and more evenly spread within and around the structure. This indicates a reduced energy storage capability compared to the first resonance. Additionally, the field behind the resonator displays higher intensity levels than in Figure 4(a), suggesting that a larger portion of the incident electromagnetic energy is transmitted rather than confined within the ring. This observation aligns with the smaller attenuation contribution (−3.61 dB) obtained from the S_{21} analysis at f_{res2}. Overall, the second resonant mode exhibits weaker electromagnetic coupling and reduced field enhancement compared to the first resonance, which directly explains the lower transmission suppression observed in the corresponding S_{21} response.

Figure 4(c) shows the electric field distribution at a non-resonant frequency. In contrast to the resonant cases in Figure 4(a) and 4(b), there is no significant field concentration along the ring structure. The lack of pronounced "hot" regions (red or orange zones) indicates that the electric field magnitude remains relatively low and is uniformly distributed around the resonator. The ring does not display noticeable field confinement or energy localization, and the incident electromagnetic wave propagates with minimal interaction with the structure. This confirms that, at non-resonant frequencies, the ring does not support efficient energy storage or strong electromagnetic coupling. As a result, the resonator loses its resonant functionality outside its characteristic frequencies, acting merely as a passive scatterer with negligible influence on the overall field distribution and transmission characteristics.

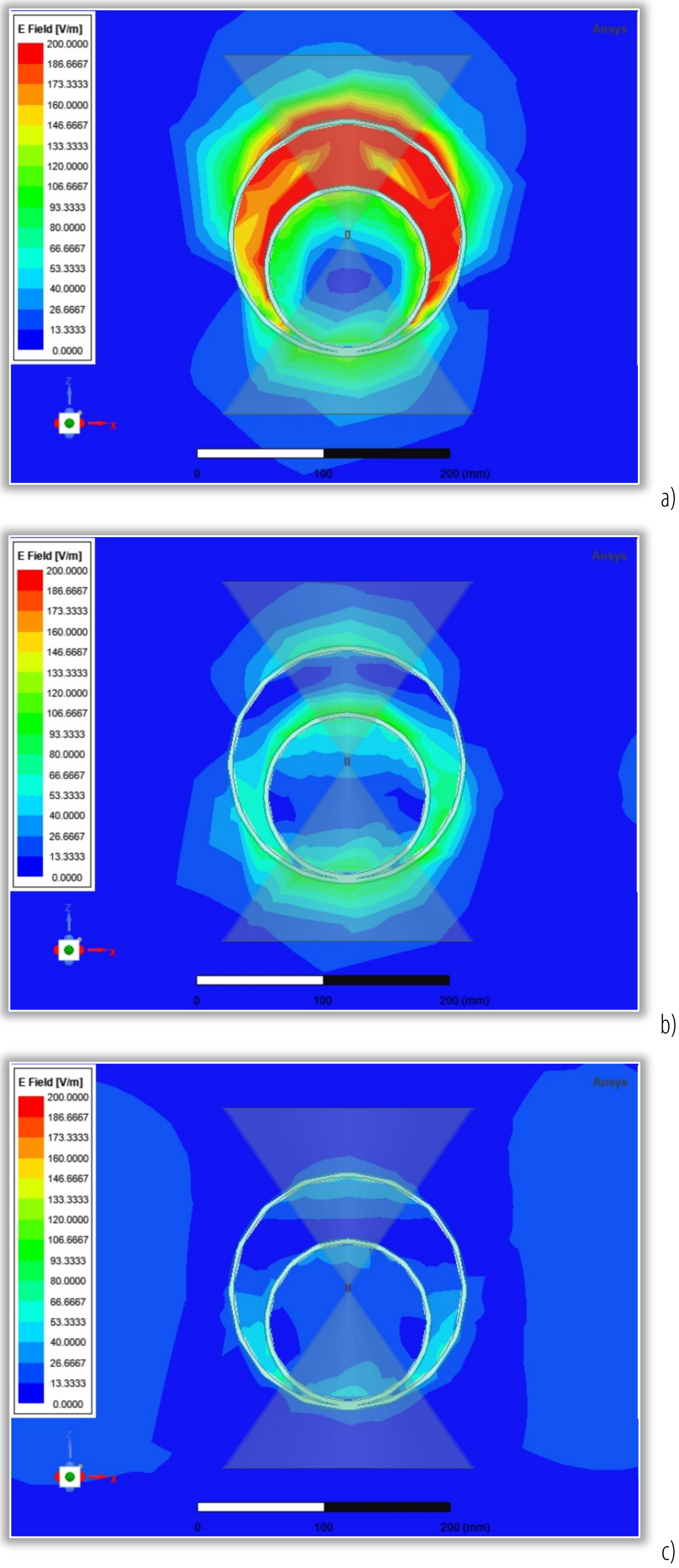

Figure 4. In-plane electric field localization and resonant behavior of an eccentric ring resonator at: a) 410.00 MHz, b) 708.00 MHz and c) 1000.00 MHz.

The horizontal (top-down) field distribution clearly shows the antenna and ring resonator system (see Figure 5). Regions of high field intensity ("hot" regions) are visible near the source (left side of the Figure 5 a)). Significant field concentration is also observed on the ring resonator, indicating

ISSN 1584 – 2665 (printed version); ISSN 2601 – 2332 (online); ISSN-L 1584 – 2665

that the ring actively participates in energy coupling. Moving away from the ring towards the receiving antenna, the field gradually decreases, as shown by the fading "hot" areas. The field at the receiving antenna is minimal, appearing as a small dot, suggesting that energy transfer is not yet maximal at this frequency.

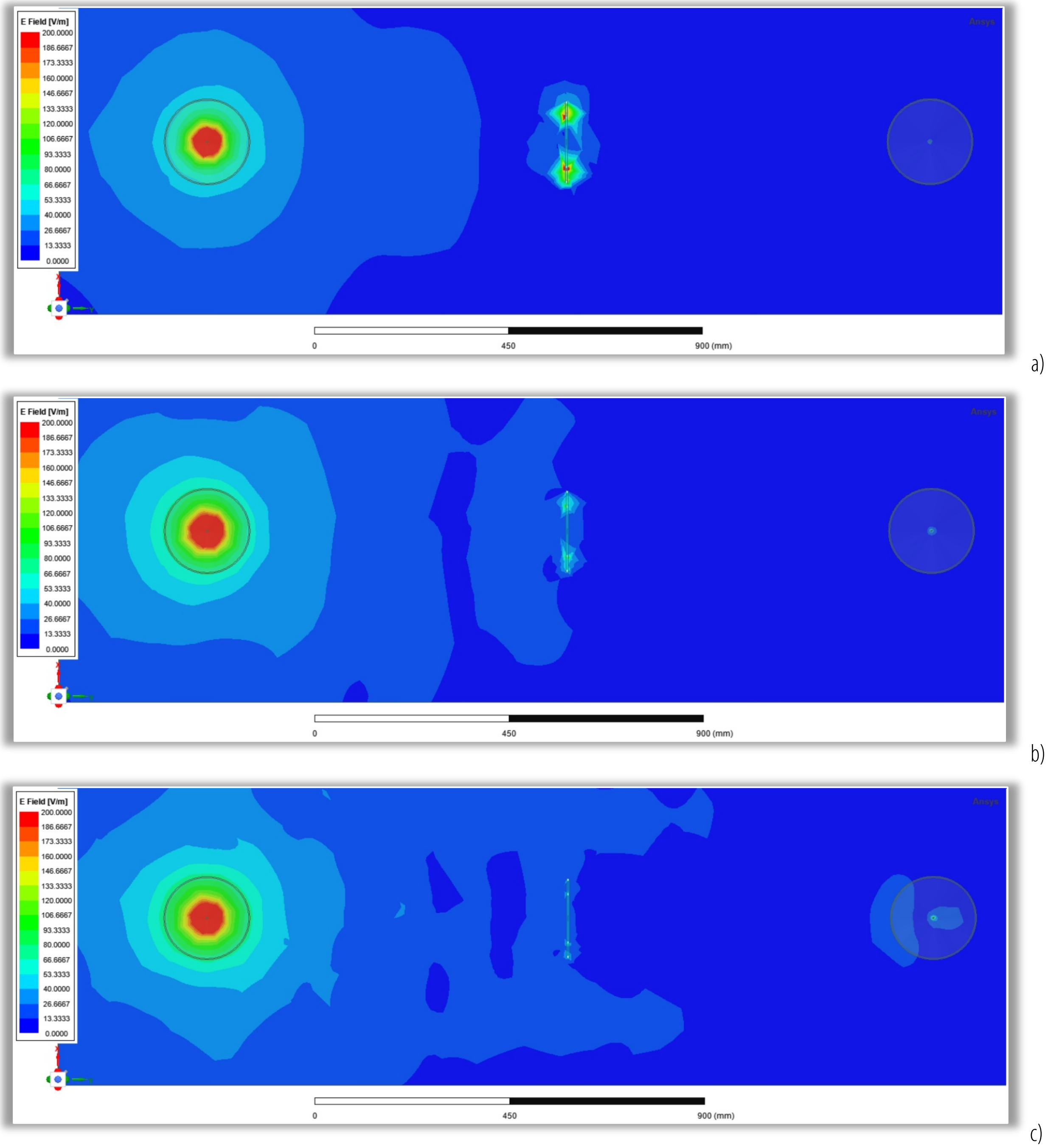

Figure 5. Electric field distribution in the horizontal plane of the ANT1—Eccentric Ring Resonator—ANT2 Configuration at:
a) 410.00 MHz, b) 708.00 MHz and c) 1000.00 MHz.

At 708.00 MHz, the electric field distribution reveals the second resonant mode of the ring resonator. Although localized "hot" regions remain observable along the ring circumference, their amplitude is significantly reduced compared to the first resonance. The field confinement is weaker, and a larger portion of the incident electromagnetic energy propagates towards the receiving antenna. This behavior indicates reduced electromagnetic coupling efficiency and lower energy storage capability at the second resonant frequency. Overall, while the ring remains excited at 708.00 MHz, the field intensity on the structure is lower than at approximately 410.00 MHz, and energy transmission towards the receiving antenna is more pronounced (Fig. 5(b)).
At 1000.00 MHz, which is well outside the resonant regime, the field distribution changes fundamentally. The electric field is no longer concentrated on the ring but is instead more uniformly distributed, indicating predominantly scattering behavior rather than resonant

confinement. Only weak excitation of the ring is observed, confirming that the structure does not operate as an efficient resonator at this frequency. A portion of the field propagates directly towards the receiving antenna, where a moderate field concentration is visible. Compared to the resonant cases, the system exhibits reduced energy localization and increased transparency to the incident wave. These observations demonstrate that, as the operating frequency moves away from resonance, field confinement on the ring diminishes, while direct energy transfer through the system becomes more significant (Fig. 5(c)).

The vertical (side) view further clarifies the mechanism of field propagation from the transmitting antenna (Tx), through the ring resonator, to the receiving antenna (Rx).

Figure 6(a) corresponds to the first resonant frequency (f_{res1} = 410.00 MHz). At this frequency, strong excitation of the ring is evident, with pronounced energy localization on the resonator and only a limited fraction of the field reaching the receiving antenna. This confirms the dominant energy trapping mechanism at the fundamental resonance.

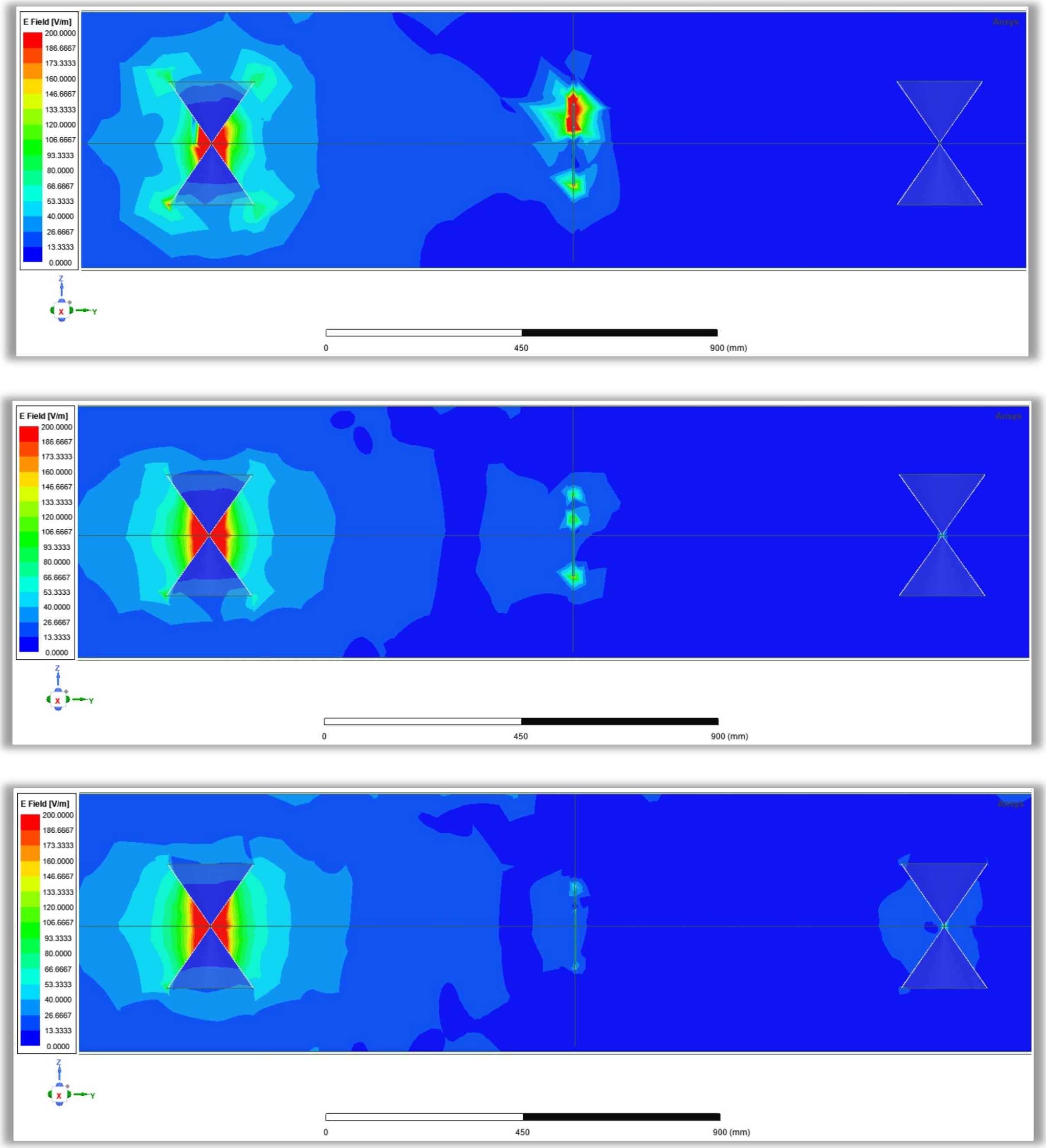

a)

b)

c)

Figure 6. Electric field strength distribution in the vertical plane of the model: ANT1 - Eccentric ring resonator - ANT2 at:
a) 410.00 MHz, b) 708.00 MHz and c) 1000.00 MHz.

Figure 6(b) illustrates the second resonant frequency (f_{res2} = 708.00 MHz). The ring is again excited; however, the confinement effect is weaker than in the first resonance. A more substantial portion of the electromagnetic energy propagates towards the receiving antenna, although significant field concentration remains on the resonator.

Figure 6(c) presents the field distribution at a non-resonant frequency (f_{non_res} = 1000.00 MHz). In this regime, the ring does not exhibit resonant behavior, and the electric field propagates with minimal interaction with the structure. Consequently, the receiving antenna experiences the highest field intensity among the three cases, while the ring itself shows negligible excitation. The system therefore behaves in a quasi-transparent manner, with the resonator no longer acting as an energy-trapping element.

The vertical-plane field distributions clearly demonstrate the governing role of the ring resonator in mediating energy transfer between the antennas. At resonant frequencies, electromagnetic energy is efficiently confined and localized on the structure, resulting in reduced transmission. In contrast, outside the resonant regime, energy confinement diminishes and direct field propagation towards the receiving antenna becomes dominant.

In summary, Figs. 4–6 collectively provide a comprehensive and physically consistent interpretation of the electric field behavior within the ring resonator system over the analyzed frequency range.

Figure 4 shows the in-plane field concentration directly on the ring at 410.00 MHz, 708.00 MHz, and 1000.00 MHz. The results clearly indicate maximum energy localization at the first resonant frequency (f_{res1}), reduced but still observable confinement at the second resonance (f_{res2}), and negligible field concentration at the non-resonant frequency. At resonance, the ring functions as an efficient energy-storage element, whereas outside the resonant regime it no longer exhibits pronounced electromagnetic confinement.

Figure 5, presenting the horizontal-plane distribution, further clarifies the transmission mechanism between the transmitting and receiving antennas. At resonant frequencies, the field is predominantly localized around the ring, limiting the amount of energy that propagates towards the receiver. In contrast, at the non-resonant frequency, the structure becomes increasingly transparent to the incident wave, enabling more efficient energy transfer to the receiving antenna.

Figure 6 provides complementary insight through the vertical-plane perspective, revealing the propagation pathway of the electric field from the transmitting antenna (Tx), through the resonant structure, to the receiving antenna (Rx). The plots confirm that, at resonant frequencies, electromagnetic energy is largely confined within the resonator, thereby reducing transmitted field intensity. Conversely, off-resonance, the absence of effective field trapping allows more direct propagation, resulting in the highest electric field levels at the receiving antenna.

Results clearly demonstrate the frequency-dependent electromagnetic response of the eccentric ring resonator. The structure acts as an energy-confining and attenuating element at its characteristic resonant frequencies, while outside this regime it transitions towards a weakly interacting, quasi-transparent scatterer. This dual behavior highlights the resonator's selective filtering capability and confirms its potential applicability in frequency-selective attenuation and shielding systems.

6. CONCLUSION

This study demonstrates a frequency-dependent electromagnetic behavior of an eccentric ring resonator positioned between a transmitting and a receiving antenna. The interaction between resonance, energy confinement, and field propagation were systematically examined by the means of full-wave numerical simulations. To ensure physically consistent modelling of the field coupling mechanisms across both resonant and non-resonant frequency regimes, the geometrical parameters of the ring, material properties, and antenna configuration were precisely defined.

Results reveal a pronounced resonance-controlled response of the system. At the first resonant frequency (f_{res1} = 410.00 MHz), the ring exhibits strong electromagnetic excitation and significant energy localization, effectively trapping the incident energy and minimizing transmission towards the receiving antenna. At the second resonance (f_{res2} = 708.00 MHz) the confinement effect remains present, but it is weaker, resulting in increased energy transfer to the receiver. In contrast, at the non-resonant frequency (f_{non_res} = 1000.00 MHz), the resonator no longer supports efficient energy storage, and the structure behaves as a weakly interacting scatterer, allowing the strongest field intensity to reach the receiving antenna.

This resonance-governed behavior was consistently confirmed through three complementary perspectives: (i) direct field concentration on the ring structure, (ii) horizontal-plane field

ISSN 1584 – 2665 (printed version); ISSN 2601 – 2332 (online); ISSN-L 1584 – 2665

distribution across the transmission path, and (iii) vertical-plane mapping of field propagation between the antennas. The consistency among these analyses provides a coherent and physically transparent interpretation of the attenuation and transmission mechanisms observed in the S_{21} response.

The findings clearly show that the eccentric ring resonator functions as a frequency-selective energy mediator, capable of strong field confinement at resonance and quasi-transparent transmission off-resonance. Such dual behavior highlights its applicability in frequency-selective attenuation, filtering, shielding, and controlled energy-routing systems. In addition, the results indicate that off-resonant operation can be strategically exploited to enhance direct transmission, offering potential advantages in tunable or broadband electromagnetic environments.

Future research may extend this work towards coupled resonator networks or array configurations, where collective resonance effects could further enhance confinement, selectivity, and controllable energy transfer. Investigation of reconfigurable geometries or active materials could potentially enable adaptive and tunable electromagnetic responses. Finally, experimental validation of the proposed configurations would provide additional confirmation of the numerical findings and support their practical implementation in advanced wireless, sensing, and electromagnetic compatibility applications.

LITERATURA:

[1] Z. Liu, J. Duan, and X. Wang, "Shielding Performance of Electromagnetic Shielding Fabric Implanted with 'Split-Ring Resonator'," Polymers, vol. 15, no. 6, art. no. 1366, 2023.
[2] I. Royo, R. Fernández-García, and I. Gil, "Microwave resonators for wearable sensors design: A systematic review," Sensors, vol. 23, no. 22, art. no. 9103, 2023.
[3] S. K. Ibrahim, S. S. Al-Bawri, M. J. Singh, H. H. Ibrahim, M. T. Islam, M. S. Islam, W. M. Abdulkawi, and A.-F. A. Sheta, "Compact metamaterial-based single/double-negative/near-zero index resonator for 5G sub-6 GHz wireless applications," Scientific Reports, vol. 14, art. no. 12834, 2024.
[4] T. J. Boland, C. Nelson, H. ElBidweihy, and C. S. Smith, "Additive manufacturing of complementary split ring resonator frequency selective surfaces," Rapid Prototyping Journal, pp. 1–8, 2025
[5] S. M. I. Huq, G. Xiao, and S. Bhadra, "Printed split ring resonator based microwave sensor on biodegradable substrate for dielectric characterization," Sensors and Actuators A: Physical, vol. 393, art. no. 116856, 16 Oct. 2025.
[6] M. R. Islam, M. T. Islam, A. Hoque, B. Bais, H. Alsaif, M. S. Islam, and M. S. Soliman, "Quad-band split ring resonator-based sensor for microwave sensing application," Scientific Reports, vol. 15, art. no. 6888, 2025.
[7] M. Idrees, Y. He, Y. Wen, and A. Majeed, "Design of a Miniaturized and Polarization-Independent Frequency-Selective Surface for Targeted EMI Shielding," Applied Sciences, vol. 15, no. 8, art. no. 4534, 2025
[8] N. Meka and K. Shambavi, "Design of conformal dual stop band frequency selective surface for microwave applications," Physics Open, vol. 26, Feb. 2026, art. no. 100352.
[9] H. Ali, B. T. Malik, L. Riaz, M. F. Shafique, and S. Koziel, "Multi-band frequency selective metasurface based filter for WLAN and X-band EMI shielding applications," Scientific Reports, vol. 15, art. no. 22297, 2025.
[10] S. Rupčić, V. Mandrić, and I. Baxhaku, "Analytical, numerical, and experimental investigation of an eccentric double-ring microwave resonator for electromagnetic shielding applications," Applied Sciences, vol. 15, art. no. 12928, 2025.

ISSN 1584 – 2665 (printed version); ISSN 2601 – 2332 (online); ISSN-L 1584 – 2665